A Rigorous Model Order Reduction Framework for Waste Heat Recovery Systems Based on Proper Orthogonal Decomposition and Galerkin Projection

Bin Xu ⓘ, Adamu Yebi ⓘ, Mark Hoffman ⓘ, and Simona Onori ⓘ, *Member, IEEE*

Abstract—A proper orthogonal decomposition (POD) and Galerkin projection-based model order reduction framework is developed for the evaporator heat exchanger in heavy-duty diesel engine organic Rankine cycle waste heat recovery system. The dynamics in the heat exchanger are first modeled by a finite-volume model, composed of highly nonlinear, coupled, partial differential equations, and then used to generate snapshots from which basis functions are defined. Reduced order models (ROMs) are then derived using the Galerkin projection approach. The accuracy and the execution time of different POD ROMs are evaluated against the high-fidelity finite-volume model. The results show that the POD ROM dimension can be selected based on the specific requirements of accuracy and computation time demanded by the intended model utilization. The proposed ROM framework can be utilized to generate ROMs with various dimensions for different purposes, such as estimator design, model-based control, and benchmark generation.

Index Terms—Galerkin projection, heat exchanger, organic Rankine cycle (ORC), proper orthogonal decomposition (POD), reduced order model (ROM).

NOMENCLATURE

WHR	Waste heat recovery.
ORC	Organic Rankine cycle.
POD	Proper orthogonal decomposition.
ROM	Reduced order model.
FVM	Finite-volume method.
MBM	Moving boundary method.
ODE	Ordinary differential equation.
PDE	Partial differential equation.
SVD	Singular value decomposition.
CSVL	Constant speed variable load.
CAN	Controller area network.
T	Temperature (K).
ρ	Density (kg/m^3).
A	Heat transfer area (m^2).
h	Working fluid enthalpy (J/kg).
C_p	Heat capacity (J/kg/K).
$\dot{m}$	Mass flow rate (kg/s).
L	Length (m).
U	Heat transfer coefficient (J/m^2/s).
V	Volume (m^3).
m	Number of cells utilized in the FVM.
n	Time step.
p	Minimum of m and n.
q	Number of states for the reduced order model.
u	Left singular vector.
v	Right singular vector.
$X(z,t)$	Matrix with dimension of m by n.
$a_i(t)$	ith temporal coefficient.
$\phi_i(z)$	ith basis function.
$\xi_i(z)$	ith weighting function.
$\psi(z)$	Basis function to be identified.
λ	Eigenvalue.
σ	Singular value.
ϵ	Percentage error between FVM and POD ROM (%).
RMSE	Root mean square error between FVM and POD ROM.
SDE	Standard deviation error.
z	Location in flow axis direction (m).
t	Time (s).

Subscript.

f	Working fluid.
w	Tube wall between working fluid and exhaust gas.
g	Exhaust gas.

B. Xu is with the Department of Automotive Engineering, Clemson University, Greenville, SC 29607 USA (e-mail: xbin@clemson.edu).

A. Yebi was with the Department of Automotive Engineering, Clemson University, Greenville, SC 29607 USA. He is now with Mercedes-Benz Research & Development North America, Redford, MI 48239 USA (e-mail: ayebi@clemson.edu).

M. Hoffman is with the Department of Mechanical Engineering, Auburn University, Auburn, AL 36849 USA (e-mail: mhoffman@auburn.edu).

S. Onori is with the Energy Resources Engineering Department, Stanford University, Stanford, CA 94305 USA (e-mail: sonori@stanford.edu).

I. INTRODUCTION

IN THE past decade, WHR technology has become increasingly popular in the automotive industry for its potential to improve fuel economy and reduce emissions [1]. Typical brake thermal efficiency values for gasoline and diesel engines are below 40% and 50%, respectively. Thus, the majority of the fuel energy is wasted as heat, which is the potential energy source to improve engine efficiency.

WHR technology generates electricity or produces mechanical power from waste heat sources such as the tail pipe exhaust gas, exhaust gas recirculation, charge air, and engine coolant [2]. Three WHR technologies have been pursued so far: turbo compounding, thermoelectric generation,
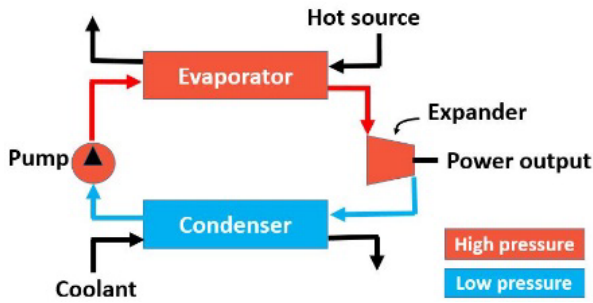
Fig. 1. ORC diagram.

and ORCs. Even though ORC systems involve the most complicated system architecture of the three WHR technologies and are relatively costly, they have become a widespread research area due to their high efficiency and mature utilization in industrial applications [3].

The ORC-WHR system includes four main components: a pump, two heat exchangers (an evaporator and a condenser), and an expander in Fig. 1. The pump circulates the working fluid through the cycle. Working fluid emanating from the pump flows into the evaporator, absorbs heat from the heat source, and undergoes a phase change from liquid to mixed (a mixture of liquid and vapor phases) and finally to vapor phase. High-pressure vapor subsequently passes through the expander and produces electricity or mechanical power. After the expander, the low-pressure vapor flows into the condenser and rejects enough heat to return to liquid phase, concluding the cycle.

The heat exchanger model involves multiphysics phenomena, namely, the phase change of the working fluid among the liquid, mixed, and vapor phases, and conservation of mass and energy. The interaction of these multiphysics phenomena is modeled by coupled nonlinear PDEs [4]. During the equation solving process, the PDEs are converted to ODEs. In the ORC-WHR system, most of the system states are contained within the heat exchanger model. This brief focuses on the model order reduction of the heat exchanger. The heat exchanger dynamics remains the same whether the exchanger is utilized as an evaporator or a condenser. Therefore, this brief focuses only on the modeling of an evaporator to avoid duplication.

In the literature, MBM is the most widely researched control-oriented heat exchanger model owing to its low state dimension and satisfactory accuracy. However, it suffers from numerical stability issues due to phase changes at the exit of the working fluid flow path [5]. The core of MBM is to calculate the boundaries of different working fluid phases. Based on the working fluid operating condition, there are three scenarios: 1) pure liquid phase without any boundary; 2) pure liquid phase plus mixed phase with only liquid mixed phase boundary; and 3) pure liquid phase, mixed phase, and pure vapor phase with two-phase boundaries (boundary 1—pure liquid and mixed phase boundary and boundary 2—mixed and pure vapor phase boundary). Each scenario corresponds to one model, thus there are three models under the MBM. In most cases, switching between models results in numerical instability due to poor initialization as the models have a

varying number of states. Nonswitching 0-D models have been considered, which utilize a single-cell finite-volume discretization [6]. The 0-D model has a maximum of three states, each corresponding to an energy balance equation. At the expense of intensive calibration effort, some degree of accuracy is possible through utilization of a 0-D model for given operating points. However, the predictions of the single-cell 0-D model largely deviate from those of the full finite-volume discretization as operation expands across the entire transient spectrum.

A physically derived, robust, control-oriented model is developed in this brief to address the numerical instability issues of the MBM and accuracy concerns of the 0-D model. Specifically, the POD-Galerkin projection method is proposed to reduce the coupled heat exchanger PDE dynamics. POD, also known as Karhunen–Loeve decomposition [7], and principal component analysis [8], have been widely used in model reduction of PDE systems [9]. The POD-Galerkin projection-based ROM inherits system dynamics from a snapshot produced by the FVM model. The resulting ROM inherits its accuracy from the high-fidelity, physics-based FVM model. The dimension of the state of the POD-Galerkin derived control-oriented model can be chosen based on the specific requirements of accuracy and computational cost demanded by the proposed ROM utilization. This leads to the creation of a versatile control-oriented modeling framework helpful for a variety of needs: estimator design [10], model predictive control development [11], and optimal control benchmark generation [12]. Estimator design requires high-model accuracy, whereas model predictive control would prefer a model with moderate model accuracy but low computation cost due to the real-time execution. Finally, for benchmark generation, a low computational cost model is required but accuracy must not be too low, or the results will be nonoptimal. A lumped model is usually used when implementing dynamic programing (DP) for benchmark generation, as it addresses the dimensionality issues DP suffers from.

This brief is organized as follows. Section II overviews the existing heat exchanger models, which form a basis of comparison for the proposed POD-Galerkin ROMs. Section III presents the POD ROM derivation. In Section IV, the POD ROM simulation results are provided, the accuracy and computational cost analyses are discussed. This brief ends with the conclusions in Section V.

Notation: The following notation is utilized in this brief. A matrix U is a unitary matrix if it has a relationship with its conjugate transpose U^* as follows:

$$U^*U = UU^* = I.$$

Given a matrix $X \in \mathbb{R}^{m \times n}$ with rank $p = \min(m, n)$, from the SVD method, there exist real numbers $\sigma_1 \geq \ldots \geq \sigma_p > 0$ and unitary matrices $U \in \mathbb{R}^{m \times m}$ and $V \in \mathbb{R}^{n \times n}$ such that

$$U^*XV = \Sigma = \begin{cases} [\Sigma_p | 0], & (m < n) \\ [\Sigma_p], & (m = n) \\ \left[\dfrac{\Sigma_p}{0}\right], & (m > n) \end{cases}$$

where $\Sigma_p = \mathrm{diag}(\sigma_1, \ldots, \sigma_p) \in \mathbb{R}^{p \times p}$ and the positive numbers σ_i are called singular values of X. From [7], $U = (u_1, \ldots, u_m)$ and $V = (v_1, \ldots, v_n)$. $u_i \in \mathbb{R}^{m \times 1}$ are called the left singular vectors and $v_i \in \mathbb{R}^{n \times 1}$ are called the right singular vectors, which satisfy

$$X v_i = \sigma_i u_i.$$

The inner product is defined as $\langle \cdot, \cdot \rangle$.

II. FINITE-VOLUME MODEL

Within the evaporator, heat transfers from the exhaust gas to the tube wall and then to the working fluid. The energy balance in working fluid, wall, and exhaust gas are expressed as follows.

1) Working fluid energy balance

$$\rho_f V_f \frac{\partial h_f(z, t)}{\partial t} = -\dot{m}_f L \frac{\partial h_f}{\partial z} + A_f U_f (T_w - T_f). \quad (1)$$

2) Wall energy balance

$$\rho_w C_{pw} V_w \frac{\partial T_w(z, t)}{\partial t} = k_w A_w L \frac{\partial T_w}{\partial z} - A_f U_f (T_w - T_f) \\ - A_g U_g (T_w - T_g). \quad (2)$$

3) Exhaust gas energy balance

$$\rho_g C_{pg} V_g \frac{\partial T_g(z, t)}{\partial t} = \dot{m}_g C_{pg} L \frac{\partial T_g}{\partial z} + A_g U_g (T_w - T_g). \quad (3)$$

In (1)–(3), $h_f(z, t) \in \mathbb{R}$, $T_w(z, t) \in \mathbb{R}$ and $T_g(z, t) \in \mathbb{R}$ denote the dynamic states, $z \in [0, L]$ is the spatial coordinate in the axial direction, and $t \in [0, \infty]$ is time. Refer to the nomenclature section for a description of the symbols. These three governing equations are constructed based on the following assumptions: 1) the heat conduction in the axial direction of the evaporator is neglected for all three media (working fluid, wall, and exhaust gas) and 2) the wall temperature in the radial direction is assumed to be uniform. Temporal dynamics in the exhaust gas $\rho_g C_{pg} V_g (\partial T_g / \partial t)$ in (3) is neglected due to their fast transient characteristics, resulting in

$$0 = \dot{m}_g C_{pg} L \frac{dT_g}{dz} + A_g U_g (T_w - T_g). \quad (4)$$

During the equation solving process, the PDEs are converted to ordinary ODEs based on FVM, which discretizes the entire volume into smaller, finite, and uniform volumes. FVM is similar to the finite-element method [13], except that volumes are considered rather than grid points. The governing equations are solved inside each finite volume and adjacent volumes are linked by boundary conditions. The heat exchanger is discretized into "m" uniformly volumetric cells (see Fig. 2) in the axial fluid flow direction. In each cell, the exhaust heat is absorbed by the wall and released to the working fluid. From the 1st cell to the mth cell, the working fluid changes phase from pure liquid to mixed, and finally pure vapor. The boundary conditions of the working fluid and exhaust gas are similar and are specified as mass flow and temperature at the inlet and pressure at the outlet. For the wall boundary conditions, the inlet of 1st cell and outlet of
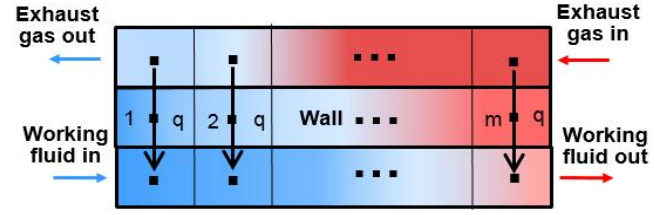

Fig. 2. Schematic of heat exchanger system when modeled via FVM using m uniform volumetric cells. In each cell, the heat flows from the exhaust gas through the wall to working fluid. In this counterflow design, the exhaust gas flows from right to left and the working fluid flows from left to right.
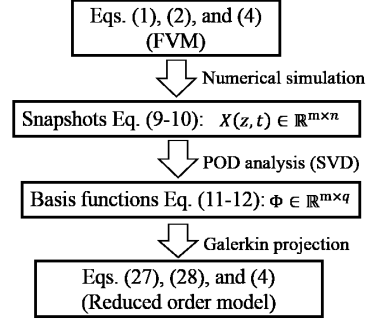

Fig. 3. POD-Galerkin ROM derivation procedures: heat exchanger PDEs generate snapshots utilizing the FVM simulation. Subsequently, POD analysis utilizes the SVD method to extract basis functions from the snapshots. Finally, the Galerkin projection minimizes residuals between the FVM and ROM, and low-order ODEs are derived.

mth cell are considered adiabatic. From the energy balance in the working fluid (1), and in the wall (2), each cell has two states, namely, the working fluid enthalpy and the wall temperature, i.e., (h_f, T_w). Thus, the FVM produces an ODE system of dimension "$2m$". The FVM is utilized to generate snapshots for the ROM in this brief. More details about the FVM ORC-WHR system can be found in [4].

III. POD-GALERKIN PROJECTION FOR HEAT EXCHANGER MODEL

The POD-Galerkin reduction process flow is shown in Fig. 3. An assumption is made before the reduced model derivation: the temporal dynamics of exhaust gas is ignored. Thus, the new derived reduced model is only valid without exhaust gas temporal dynamics. The execution of (1), (2), and (4) using the FVM generates snapshot $X \in \mathbb{R}^{m \times n}$. A snapshot consists of a column vector that describes the state within each volume of the FVM along the entire evaporator length at each instant of time, the number of columns in X, n represents the number of snapshots and the number of rows, m represents the number of elements in each snapshot. More specifically, the matrix of snapshots taken from working fluid enthalpy dynamics is indicated as $X_{h_f} \in \mathbb{R}^{m \times n}$ and the matrix of snapshots taken from wall temperature dynamics is indicated as $X_{T_w} \in \mathbb{R}^{m \times n}$. SVD is applied to extract independent, low-order basis functions from the snapshots. The SVD definition is given in the notation. Basis functions can be chosen based on the eigenvalues of the dynamic system such that the state dimension of the model can be reduced.

The basis functions are expressed as $\Phi = [\phi_1, \phi_2, \ldots, \phi_p]$. Working fluid enthalpy and wall temperature have their own basis functions $\Phi_{h_f} = [\phi_{h_f,1}, \phi_{h_f,2}, \ldots, \phi_{h_f,q_{h_f}}]$ and $\Phi_{T_w} = [\phi_{T_w,1}, \phi_{T_w,2}, \ldots, \phi_{T_w,q_{T_w}}]$, respectively. From these basis functions, the Galerkin projection minimizes the residuals between the original infinite PDE to the reduced ODE model [14]. In the following, Section III-A presents the POD analysis, which generates basis functions utilizing SVD. Section III-B presents the Galerkin projection method.

A. POD Basis Function Generation

To create the basis functions, snapshots of the system states are required. The general form of a snapshot is in the form of a matrix $X \in \mathbb{R}^{m \times n}$. Utilizing the SVD, basis functions Φ are obtained from the matrix U. Following the notation at the end of Section I, the first p columns of U are the orthogonal POD basis functions ($\Phi \in \mathbb{R}^{m \times p}$), described as:

$$\Phi = (\phi_1, \ldots, \phi_p) = (u_1, \ldots, u_p) \tag{5}$$

where each basis function ϕ_i is a column vector of m elements, i.e., $\phi_i = u_i \in \mathbb{R}^{m \times 1}$. By choosing an orthonormal basis of eigenvectors $(v_1, \ldots, v_n)$, the p basis functions can be expressed as follows:

$$u_i = \frac{1}{\sigma_i} X v_i, \quad i = 1, \ldots, p \tag{6}$$

where each u_i vector satisfies the orthonormality property [7]

$$|u| = 1 \text{ and } \langle u_i, u_j \rangle = 0, \quad j \neq i. \tag{7}$$

Thus, each basis function ϕ_i inherits the orthogonal property as follows:

$$|\phi| = 1 \text{ and } \langle \phi_i, \phi_j \rangle = 0, \quad j \neq i. \tag{8}$$

Solving (1), (2), and (4), two sets of snapshots can be obtained reflecting the working fluid enthalpy states (h_f) and the wall temperature states (T_w), respectively, as follows:

$$X_{h_f} = \begin{pmatrix} x_{h_f,1}(t_1) & \cdots & x_{h_f,1}(t_n) \\ \vdots & \ddots & \vdots \\ x_{h_f,m}(t_1) & \cdots & x_{h_f,m}(t_n) \end{pmatrix} \in \mathbb{R}^{m \times n} \tag{9}$$

$$X_{T_w} = \begin{pmatrix} x_{T_w,1}(t_1) & \cdots & x_{T_w,1}(t_n) \\ \vdots & \ddots & \vdots \\ x_{T_w,m}(t_1) & \cdots & x_{T_w,m}(t_n) \end{pmatrix} \in \mathbb{R}^{m \times n}. \tag{10}$$

In the final ROMs, the number of basis functions for the working fluid and wall is q_{h_f} and q_{T_w}, respectively. Basis functions for working fluid enthalpy and wall temperature can be expressed as

$$\Phi_{h_f} = (\phi_{h_f,1}, \ldots, \phi_{h_f,q_{h_f}}) \in \mathbb{R}^{m \times q_{h_f}} \tag{11}$$

$$\Phi_{T_w} = (\phi_{T_w,1}, \ldots, \phi_{T_w,q_{T_w}}) \in \mathbb{R}^{m \times q_{T_w}}. \tag{12}$$

B. Galerkin Projection

The spatial-temporal variables $h_f(z,t)$ and $T_w(z,t)$ from the evaporator heat exchanger model can be approximated using Fourier series [15]. Based on the Fourier series, $h_f(z,t)$ and $T_w(z,t)$ are expanded by a set of basis functions $\{\phi_{h_f,i}\}_{i=1}^{\infty}$ and $\{\phi_{T_w,i}\}_{i=1}^{\infty}$, respectively, as follows:

$$h_f(z,t) = \sum_{i=1}^{\infty} h_{f,i}(t)\phi_{h_f,i}(z) \tag{13}$$

$$T_w(z,t) = \sum_{i=1}^{\infty} T_{w,i}(t)\phi_{T_w,i}(z). \tag{14}$$

Equations (13) and (14) can be approximated as follows:

$$\sum_{i=1}^{\infty} h_{f,i}(t)\phi_{h_f,i}(z) = \overline{\phi_{h_f}^T}(z)\overline{h_f}(t) \tag{15}$$

$$\sum_{i=1}^{\infty} T_{w,i}(t)\phi_{T_w,i}(z) = \overline{\phi_{T_w}^T}(z)\overline{T_w}(t) \tag{16}$$

where $\overline{\phi_{h_f}}(z)$, $\overline{h_f}(t)$, $\overline{\phi_{T_w}}(z)$, and $\overline{T_w}(t)$ are vectors, $\overline{h_f}(t)$ and $\overline{T_w}(t)$ aretemporal states. The basis functions are ordered from slow to fast dynamics [16], where the fast modes contribute little to the system dynamics and only the first q_{h_f} and q_{T_w} slow modes are retained in working fluid and wall, respectively, [17]

$$h_{f,q_{h_f}}(z,t) = \sum_{i=1}^{q_{h_f}} h_{f,i}(t)\phi_{h_f,i}(z) = \overline{\phi_{h_f,q_{h_f}}^T}(z)\overline{h_{f,q_{h_f}}}(t) \tag{17}$$

$$T_{w,q_{T_w}}(z,t) = \sum_{i=1}^{q_{T_w}} T_{w,i}(t)\phi_{T_w,i}(z) = \overline{\phi_{T_w,q_{T_w}}^T}(z)\overline{T_{w,q_{T_w}}}(t) \tag{18}$$

where $\overline{\phi_{h_f,q_{h_f}}}(z) \in \mathbb{R}^{1 \times q_{h_f}}$, $\overline{h_{f,q_{h_f}}}(t) \in \mathbb{R}^{q_{h_f} \times 1}$, $\overline{\phi_{T_w,q_{T_w}}}(z) \in \mathbb{R}^{1 \times q_{T_w}}$, and $\overline{T_{w,q_{T_w}}}(t) \in \mathbb{R}^{q_{T_w} \times 1}$ are vectors. Thus, the spatial-temporal variable $h_f(z,t)$ is separated into a set of basis functions $\overline{\phi_{h_f,q_{h_f}}}(z)$ and the temporal variables $\overline{h_{f,q_{h_f}}}(t)$. Similarly, the spatial-temporal variable $T_w(z,t)$ is separated into a set of basis functions $\overline{\phi_{T_w,q_{T_w}}}(z)$ and the temporal variables $\overline{T_{w,q_{T_w}}}(t)$.

What has been addressed above is the time-space separation. On the contrary, if the $\overline{\phi_{h_f,q_{h_f}}}(z)$ and $\overline{h_{f,q_{h_f}}}(t)$ are known, the $h_{f,q_{h_f}}(z,t)$ can be synthesized (recovered) using (17) [15] (the right-hand side term is known and the left-hand side term is unknown). In addition, if $\overline{\phi_{w,q_{T_w}}}(z)$ and $\overline{T_{w,q_{T_w}}}(t)$ are known, $T_{w,q_{T_w}}(z,t)$ can be synthesized (recovered) using (18).

From (1), (2), (17), and (18), one can define the working fluid enthalpy residual, $R_{h_f}(z,t)$, and the wall temperature residual, $R_{T_w}(z,t)$, functions, respectively, by substituting the truncated working fluid enthalpy expansion (17) and truncated wall temperature expansion (18) into original system

dynamics (1) and (2) [17] as follows:

$$R_{h_f}(z,t) = \rho_f V_f \frac{\partial h_{f,q_{h_f}}(x,t)}{\partial t} + \dot m_f L \frac{\partial h_{f,q_{h_f}}}{\partial z} - A_f U_f (T_{w,q_{T_w}} - T_f(h_{f,q_{h_f}})) \quad (19)$$

$$R_{T_w}(z,t) = \rho_w C_{pw} V_w \frac{\partial T_{w,q_{T_w}}}{\partial t} - k_w A_w L \frac{\partial T_{w,q_{T_w}}}{\partial z} + A_f U_f (T_{w,q_{T_w}} - T_f(h_{f,q_{h_f}})) + A_g U_g (T_{w,q_{T_w}} - T_g). \quad (20)$$

Residuals $R_{h_f}(z,t)$ and $R_{T_w}(z,t)$ can be minimized by satisfying the following equations [15]:

$$\langle R_{h_f}, \xi_{h_f,i} \rangle = 0, \quad i = 1, \ldots, q_{h_f} \quad (21)$$
$$\langle R_{h_f}, \xi_{h_f,i} \rangle = 0, \quad i = 1, \ldots, q_{T_w} \quad (22)$$

where $\{\xi_{h_f,i}(z)\}_{i=1}^{q_{h_f}}$ and $\{\xi_{T_w,i}(z)\}_{i=1}^{q_{T_w}}$ are two sets of weighting functions that minimize the working fluid enthalpy residual and wall temperature residual, respectively. Details of (21) and (22) can be found in the Appendix.

The basis functions of the heat exchanger $\{\phi_{h_f,i}\}_{i=1}^{q_{h_f}}$ and $\{\phi_{T_w,i}\}_{i=1}^{q_{T_w}}$ are chosen to be the weighting functions $\{\xi_{h_f,i}(z)\}_{i=1}^{q_{h_f}}$ and $\{\xi_{T_w,i}(z)\}_{i=1}^{q_{T_w}}$, respectively, in the Galerkin projection

$$\xi_{h_f,i}(z) = \phi_{h_f,i}(z), \quad i = 1, \ldots, q_{h_f} \quad (23)$$
$$\xi_{T_w,i}(z) = \phi_{T_w,i}(z), \quad i = 1, \ldots, q_{T_w}. \quad (24)$$

The residuals (R_{h_f}, R_{T_w}) are made orthogonal to the respective basis functions [15]. Thus, the basis functions $\{\phi_{h_f,i}\}_{i=1}^{q_{h_f}}$ and $\{\phi_{T_w,i}\}_{i=1}^{q_{T_w}}$ are existing solutions to the residual minimization (21) and (22), respectively.

The ROM derivation process consists of three steps.

Step 1: Substitute (17) and (18) into (19) and (20) and assume there is no thermal conduction within the wall. The working fluid temperature $T_f(z,t)$ and exhaust gas temperature $T_g(z,t)$ are replaced by

$$T_f(z,t) = \text{map}\left(\sum_{i=1}^{q_{h_f}} h_{f,i}(t)\phi_{h_f,i}(z), p_f\right) \quad (25)$$

$$T_g(z,t) = \frac{\dot m_g C_{pg} T_g(z+1,t) + A_g U_g \sum_{i=1}^{q_{T_w}} T_{w,i}(t)\phi_{T_w,i}(z)}{\dot m_g C_{pg} + A_g U_g}. \quad (26)$$

Step 2: Multiply both sides of equations derived from Step 1 by $\xi_{h_f,j}(z)$ and $\xi_{T_w,j}(z)$, respectively. Then, add each equation along the spatial length L and substitute (21)–(24) into the derived equations.

Step 3: Substitute the orthogonal property of the basis functions (8) into the equations derived from Step 2. Assume $\dot m_f(z) = \dot m_f(0)$ and apply $h_{f,\text{in}} = \sum_{i=1}^{q_{h_f}} h_{f,i}(t)\phi_{h_f,i}(0)$. The final form of POD ROM is derived as follows.

Working fluid ODE

$$\rho_f V_f \dot h_{f,k}(t) = -\dot m_f(0) L \sum_{i=1}^{q_{T_w}} T_{w,i}(t) \times \left[\left(\sum_{i=1}^{q_{h_f}} h_{f,i}(t)\phi_{h_f,i}\right)\phi_{h_f,k}(L) - h_{f,\text{in}}\phi_{h_f,k}(0) - \sum_{i=1}^{q_{h_f}} h_{f,i}(t)\left(\sum_{j=1}^{m}\phi_{h_f,i,j}\phi'_{h_f,k,j}\right)\right] + A_f \sum_{j=1}^{m} U_{f,j}\phi_{h_f,k,j}\left(\sum_{i=1}^{q_{T_w}} T_{w,i}(t)\phi_{T_w,i,j} - T_{f,j}(t)\right). \quad (27)$$

Wall ODE

$$\rho_w V_w C_{pw} \dot T_{w,k}(t) = -A_f \left(\sum_{i=1}^{q_{T_w}} T_{w,i}(t)\left(\sum_{j=1}^{m}\phi_{T_w,i,j}U_{f,j}\phi_{T_w,k,j}\right) - \sum_{j=1}^{m} U_{f,j}T_{f,j}(t)\phi_{T_w,k,j}\right) - A_g U_g\left(T_{w,k}(t) - \sum_{j=1}^{m} T_{g,j}(t)\phi_{T_w,k,j}\right). \quad (28)$$

The exhaust gas equation of the POD ROM is (4).

IV. SIMULATION RESULTS AND DISCUSSION

The POD-Galerkin-based reduced modeling approach is demonstrated herein. Snapshot generation is discussed in Section IV-A, while Section IV-B evaluates the computation time and accuracy of POD ROMs with different dimensions.

A. Finite-Volume Model Calibration

The snapshots are obtained from the evaporator FVM, whose parameters were identified and validated over experimental data collected in the ORC-WHR test bench at the Department of Automotive Engineering at Clemson University. The test bench utilizes a 13-L heavy-duty diesel engine coupled with the ORC-WHR system through a tail pipe exhaust gas evaporator installed downstream of the emissions after treatment system. The ORC-WHR system contains two low-pressure feed pumps, a high-pressure pump, a turbine expander, and a condenser. Further details of the experimental setup and model calibration can be found in [4].

B. Snapshot Generation

Snapshots are numerical representations of the system dynamics when subjected to a given input. In this brief, a transient engine driving cycle is the FVM input utilized to produce the simulation results, which are utilized as snapshots. Specifically, the snapshots are generated utilizing exhaust data
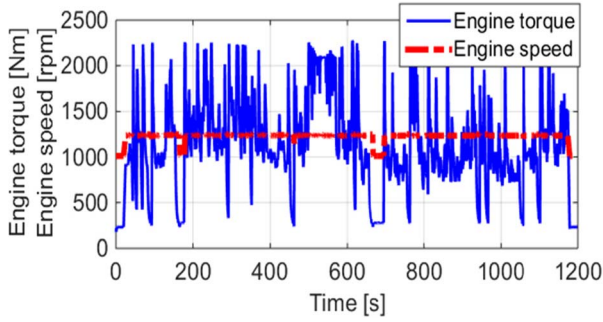
Fig. 4.   CSVL heavy-duty engine driving cycle for the snapshot generation.

Fig. 5.   Diagram of simulation data generation in the snapshot generation process. Snapshots from the CSVL driving cycle derive the POD ROM.

from a CSVL heavy-duty driving cycle. The inputs include the exhaust gas mass flow rate and temperature downstream of the emissions after treatment system, as predicted by the validated GT-POWER engine model. The CSVL driving cycle is characterized by a nearly constant engine speed around 1200 rpm and a heavily transient load profile, as shown in Fig. 4.

Note that the performance of POD ROM depends on the basis functions, which are derived from snapshots. Thus, the snapshots operating conditions are the key to POD ROM performance. Even though there is no theory to guarantee the performance of POD ROM, there are still some ways to expand the POD ROM operating conditions. For example, validate POD ROM over various driving cycles. If the errors are large in one driving cycle, this driving cycle can be added to the basis function generation condition. Moreover, the frequency of exhaust gas mass flow rate and temperature can be analyzed for different driving cycles and compare them with the driving cycle utilized in basis function generation. The POD ROM can be improved by increasing the frequency range. These methods require systematic analysis and are hardly covered with short space. Thus, they are explored in this brief.

For the snapshot generation simulation, the FVM and the POD ROM share the same boundary and initial conditions, which are given as follows. For the working fluid, the mass flow rate $\dot{m}_{f,\text{in}}$ and temperature $T_{f,\text{in}}$ are given at the evaporator inlet, while the pressure $p_{f,\text{out}}$ is given at the outlet. For the wall, as shown in Fig. 2, both the left side and right side of the heat exchanger are adiabatic. For the exhaust gas, the mass flow rate $\dot{m}_{g,\text{in}}$ and temperature $T_{g,\text{in}}$ are given at the evaporator inlet, and the pressure $p_{g,\text{out}}$ is given at the outlet.

During the simulation, the working fluid mass flow rate remains fixed at 0.029 kg/s and working fluid evaporation pressure is a constant 20 bar. The working fluid mass flow rate is chosen based on the exhaust gas power of the CSVL driving cycle so that during the entire driving cycle, all three working fluid phases exist (liquid, mixed, and vapor). The evaporation pressure is chosen based on typical operating conditions in the ORC-WHR system.

According to [4], compared with 100 discretized cells, discretization with 5, 10, 20, and 30 cells presents 10.3%, 3.4%, 1.6%, and 0.9% error, respectively. A 30 cell FVM discretization is chosen in this brief for accuracy, resulting in a 60-state FVM. This makes the FVM heat exchanger model
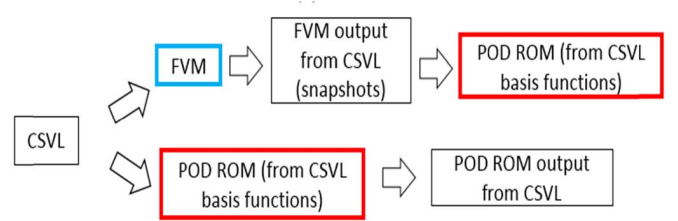
not readily applicable for real-time model-based control and estimation design purposes. To ensure the FVM convergence, an explicit solver is utilized with a small enough time step to satisfy the current conditions [18].

The snapshot generation process and POD ROM simulation process are shown in Fig. 5. Three error calculation metrics are utilized in this brief. RMSE is defined in (29), the SDE is defined in (30), and the maximum error

$$\text{RMSE} = \sqrt{\frac{1}{n}\sum_{i=1}^{n}\left(T_{\text{POD},j,m,i} - T_{\text{FVM},j,m,i}\right)^2} \tag{29}$$

$$\text{SDE} = \sqrt{\frac{1}{n-1}\sum_{i=1}^{n}(|T_{\text{POD},j,m,i} - T_{\text{FVM},j,m,i}| - \bar{e})^2} \tag{30}$$

$$\bar{e} = \frac{1}{n}\sum_{i=1}^{n}|T_{\text{POD},j,m,i} - T_{\text{FVM},j,m,i}| \tag{31}$$

where subscript j represents either working fluid, wall, or exhaust gas, subscript m represents the mth cell location along the heat exchanger, subscript i represents the ith time step.

C. Performance Evaluation of the POD ROMs

In the POD ROM, the two dynamics of interest are working fluid enthalpy and wall temperature, whose dimensions are q_{h_f} and q_{T_w}, respectively. After snapshot determination, a SVD operation is applied to the snapshot. Ordered singular values for the working fluid enthalpy ($\sigma_{h_f,1} \geq \ldots \geq \sigma_{h_f,q_{h_f}}$) and wall temperature ($\sigma_{T_w,1} \geq \ldots \geq \sigma_{T_w,q_{T_w}}$) determined from the snapshots are graphically represented in Fig. 6. For the working fluid enthalpy, note that the first singular value $\sigma_{h_f,1}$ is nearly three orders of magnitude larger than that of the second singular value $\sigma_{h_f,2}$, which reveals that the main dynamics are captured in the first singular value $\sigma_{h_f,1}$. In addition, the singular values decrease significantly as the state dimension number increases (x-axis), which means higher order singular values do not capture much of the dynamics. Thus, there is significant potential to reduce the system states. The same behavior can be observed in the wall temperature singular values.

The RMSE, maximum error, and SDE for different POD ROMs at the mth cell (the evaporator exit) are shown in Fig. 7. In Fig. 7(a), (c), and (e), q_{h_f} is fixed at 10 and q_{T_w} is swept from 1 to 10. As expected, the RMSE of working fluid and wall temperature decreases as q_{h_f} increases. The varying range of the working fluid temperature and the wall
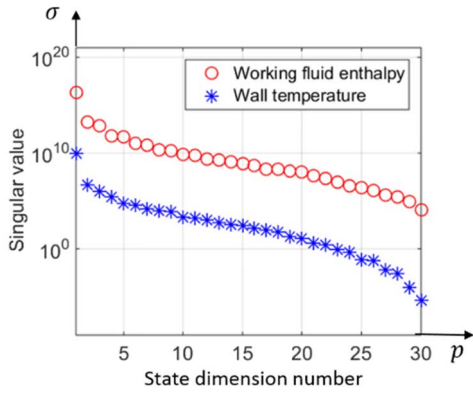
Fig. 6. Singular values of working fluid enthalpy and wall temperature calculated from the snapshot.
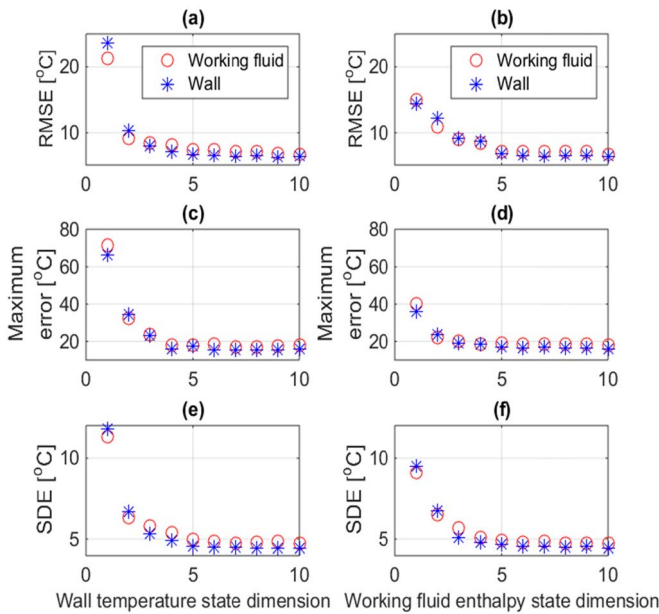

Fig. 7. RMSE, maximum error, and SDE of working fluid temperature and wall temperature for the ROM with different state dimensions. (a), (c), and (e) $q_{h_f} = 10$, q_{T_w} sweeps from 1 to 10. (b), (d), and (f) $q_{T_w} = 10$, q_{h_f} sweeps from 1 to 10.

Fig. 8. Computation time of the POD ROM state update. (a) $q_{T_w} = 10$, q_{h_f} sweeps from 1 to 10. (b) $q_{h_f} = 10$, q_{T_w} sweeps from 1 to 10.

Fig. 9. Comparison between the POD ROMs and the snapshot. (a) Working fluid outlet temperature. (b) mth wall temperature (wall temperature at the exit of the heat exchanger). In the legend, (10, 1) represents $q_{h_f} = 10$, $q_{T_w} = 1$. Only 300 s and 5 POD ROMs are plotted against snapshot for readability.

temperature is 295 °C and 217 °C, respectively. The maximum error and SDE show similar trend with RMSE. When q_{T_w} is fixed at 10 and q_{h_f} is swept from 1 to 10, the errors decrease with increasing state dimension. For each state, as the state dimension increases above five, further RMSE reduction is minimal.

The execution time for working fluid enthalpy and wall temperature states is calculated and reported in Fig. 8. The wall temperature state dimension is fixed to 10 and only the working fluid enthalpy state increases, the computation time for the working fluid enthalpy state update increases almost linearly. Moreover, when the working fluid enthalpy state dimension is fixed to 10 and only wall temperature state dimension changes. As the wall temperature state dimension increases, the computation time for the wall temperature
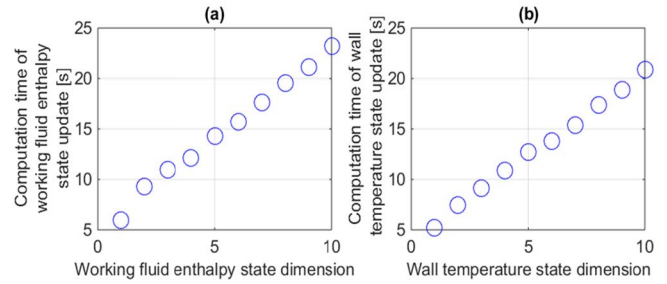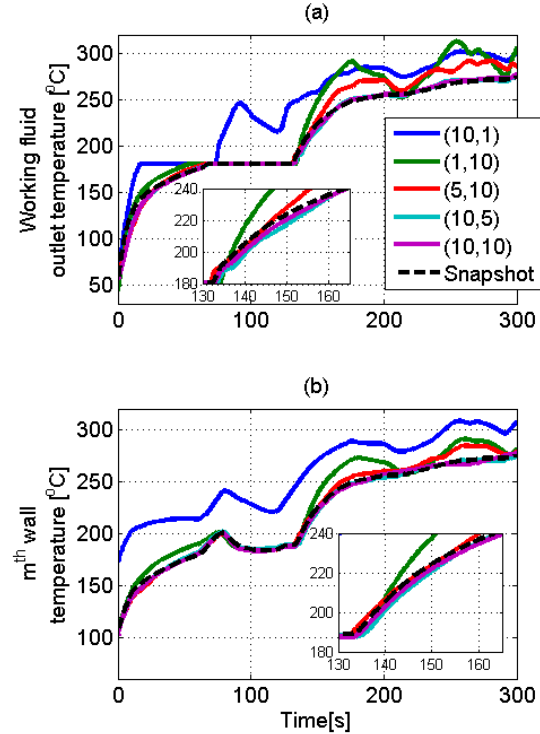
state update increases nearly linear. Therefore, for the POD ROM, fewer states require less computation time and the computation time increases nearly linear with the increase of state dimension.

Several POD ROMs are compared with the FVM snapshots as shown in Fig. 9, where 300 s of the transient simulation and five POD ROMs of different state dimensions are reported. The selected 300-s window is the most challenging portion of the entire 1200-s simulation. This time period includes a transition of the working fluid outlet conditions from liquid to mixed phase and finally to superheated vapor.

In Fig. 9(a), at the beginning of the 300-s window, the working fluid only exists in the liquid phase along the entire heat exchanger and the outlet temperature is around 50 °C. The liquid working fluid continues to warm until reaching
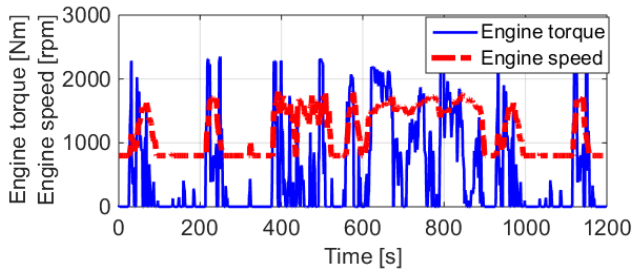
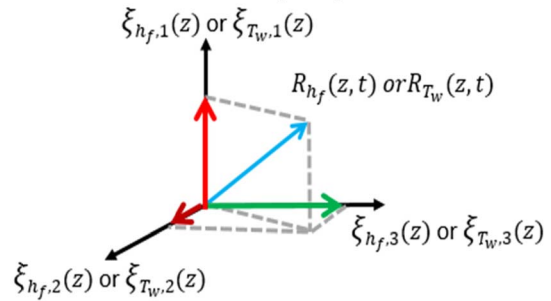Fig. 10. FTP heavy-duty engine driving cycle used for the POD ROMs validation.
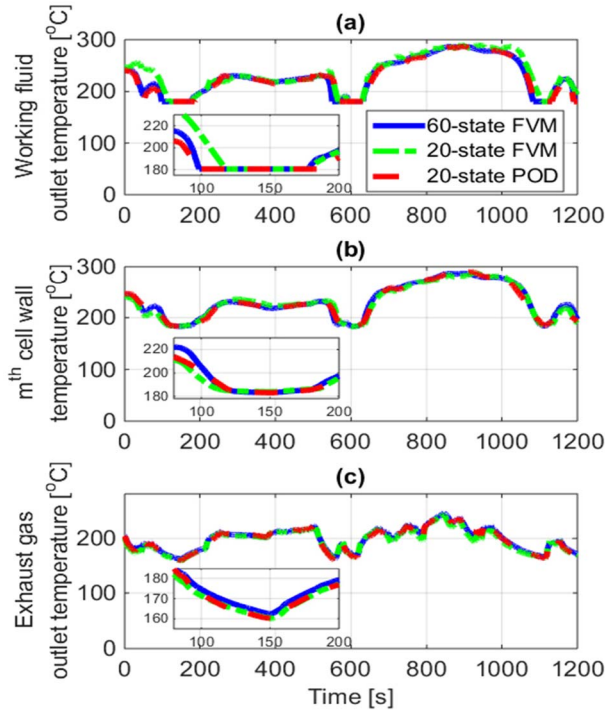

Fig. 11. Comparison between 20-state POD ROM, 20-state FVM, and 60-state FVM. (a) Working fluid outlet temperature. (b) mth wall temperature. (c) Exhaust gas outlet temperature.

Fig. 12. Geometric interpretation of weighted residual method for $q_{h_f} = q_{T_w} = 3$.

saturation (mixed phase) as shown by the horizontal line appearing. The horizontal line is due to the constant evaporation temperature at given constant evaporation pressure. The working fluid quality increases until the evaporator outlet phase is pure vapor. Additional heat input to the evaporator causes the vapor to experience superheat, and the working fluid outlet temperature starts to climb again. In the legend (a, b): a represents the dimension of enthalpy while b represents the wall temperature state dimension. POD ROMs with high state dimensions show better results than the POD ROMs with low state dimensions [(10, 5) vs. (10, 1), (5, 10) vs. (5, 10), and (10, 10) vs. (5, 10)]. Out of the five ROMs, the ROM with (10, 1) shows the worst result in both Fig. 9(a) and (b). In Fig. 9(a), the phase change of POD ROM with (10, 1) is anticipated by around 50 s before the FVM snapshot (horizontal line at 180 °C). This is due to the overpredicted POD-Galerkin wall temperature in Fig. 9(b) owing to the low-wall temperature state dimension. The high-wall temperature

overpredicts the heat transfer between the working fluid and the wall, resulting in the temporal advance of the working fluid phase change. The POD ROM with state dimension (1, 10) outperforms the POD ROM with state dimension (10, 1). This reveals that, for an 11-state ROM, wall dynamics contributes to the system dynamics more than the working fluid dynamics. However, the POD ROM with state dimension (10, 5) outperforms the POD ROM with state dimension (5, 10). Thus, for the 15-state POD ROM, working fluid dynamics contribute to the system dynamics more than the wall dynamics. Balancing the influence of the wall and working fluid enthalpy state dimensions with the total number of model states is the key for model accuracy at given computation cost. In the zoomed-in view of the inset of Fig. 9(a), the POD ROM with state dimension (10, 10) shows slightly better performance than the ROM with state dimension (10, 5). Overall, POD ROMs with state dimensions (10, 10) and (10, 5) show the good agreement with the snapshot.

The POD ROM is further validated over a different driving cycle, the federal test procedure (FTP), whose engine torque and speed traces are shown in Fig. 10. During the simulation, a 20-state FVM is compared to a 20-state POD ROM. Meanwhile, a 60-state FVM is considered as the reference. The results are shown in Fig. 11. Congruous with the results from CSVL cycle implementation, the 20-state POD ROM shows the close agreement with the benchmark 60-state FVM. The 20-state FVM and 20-state POD ROM show a similar performance on wall and exhaust gas temperature prediction. However, the 20-state POD ROM more accurately predicts the working fluid temperature. The working fluid outlet temperature RMSE of the 20-state POD ROM and 20-state FVM is 5.7 °C and 11.9 °C, respectively, while the magnitude of temperature variation during the transient is 254 °C. Similar to RMSE, the maximum error and SDE of the POD ROM are half that of the FVM results (maximum error 23.7 °C vs. 42.5 °C, SDE 4.9 °C vs. 9.5 °C). The computation time for the two models is 19.3 and 45.7 s, respectively. Given 20 states, the POD ROM shows half the FVM working fluid temperature error while consuming less than half the FVM computation time.

V. CONCLUSION

A POD-Galerkin ROM framework was proposed for the heat exchanger used in the ORC-WHR system. Snapshots were

generated utilizing the CSVL and FTP driving cycles, from a high fidelity, experimentally validated FVM. The proposed POD ROM framework was utilized to generate various ROMs with different dimensions from the FVM snapshots. Implementation results of different dimension ROMs show that computation time increased linearly with the POD ROM state dimension and the POD ROM's error decreased asymptotically as the state dimension increased. Thus, the dimension of the POD ROM can be selected based on the requirement of the application of interest. For offline simulation, high-order POD ROMs can be considered for their high accuracy. For online state estimation or other model-based control, middle to low-order POD ROMs can be considered for their low computation cost and satisfactory accuracy.

The POD ROMs developed in this brief are fully derived from the FVM simulation results without any calibration. An adaptive POD Galerkin model can be considered to reduce the errors of the POD ROMs in the future. The adaptive POD ROMs identify the heat transfer coefficients and heat exchanger efficiency using experimental data every period of time. This method can reduce the influence brought by the FVM model errors.

APPENDIX

As shown in Fig. 12, the minimization of the residual R_{h_f} is equivalent to the minimization of its projections onto weighting functions $\xi_{h_f,i}(i = 1, \ldots, q_{h_f})$. The minimization of the residual R_{T_w} is equivalent to the minimization of its projections onto weighting functions $\xi_{T_w,i}(i = 1, \ldots, q_{T_w})$. The accuracy and efficiency of the weighted residual method are dependent on the basis and weighting functions chosen [43].

REFERENCES

[1] S. Quoilin, V. Lemort, and J. Lebrun, "Experimental study and modeling of an organic rankine cycle using scroll expander," *Appl. Energy*, vol. 87, no. 4, pp. 1260–1268, Apr. 2010.

[2] S. Quoilin, M. Van Den Broek, S. Declaye, P. Dewallef, and V. Lemort, "Techno-economic survey of organic rankine cycle (ORC) systems," *Renew. Sustain. Energy Rev.*, vol. 22, pp. 168–186, Jun. 2013.

[3] B. F. Tchanche, G. Lambrinos, A. Frangoudakis, and G. Papadakis, "Low-grade heat conversion into power using organic rankine cycles—A review of various applications," *Renew. Sustain. Energy Rev.*, vol. 15, pp. 3963–3979, Oct. 2011.

[4] B. Xu *et al.*, "Transient dynamic modeling and validation of an organic rankine cycle waste heat recovery system for heavy duty diesel engine applications," *Appl. Energy*, vol. 205, pp. 260–279, Nov. 2017.

[5] J. M. Jensen, "Dynamic modeling of thermo-fluid systems: With focus on evaporators for refrigeration," M.S. thesis, Dept. Mech. Eng., Tech. Univ. Denmark, Lyngby, Denmark, 2003.

[6] J. Peralez, P. Tona, A. Sciarretta, P. Dufour, and M. Nadri, "Optimal control of a vehicular organic rankine cycle via dynamic programming with adaptive discretization grid," *IFAC Proc. Vol.*, vol. 47, pp. 5671–5678, Jan. 2014.

[7] R. Pinnau, "Model reduction via proper orthogonal decomposition," in *Model Order Reduction: Theory, Research Aspects and Applications*, vol. 13. Berlin, Germany: Springer, 2008, pp. 95–109.

[8] S. Wold, K. Esbensen, and P. Geladi, "Principal component analysis," *Chemometrics Intell. Lab. Syst.*, vol. 2, nos. 1–3, pp. 37–52, Aug. 1987.

[9] I. Kalashnikova, S. Arunajatesan, M. F. Barone, B. G. van Bloemen Waanders, and J. A. Fike, "Reduced order modeling for prediction and control of large-scale systems," Sandia Nat. Lab., Livermore, CA, USA, Tech. Rep. SAND2014-469, May 2014.

[10] A. Yebi *et al.*, "Estimation and predictive control of a parallel evaporator diesel engine waste heat recovery system," *IEEE Trans. Control Syst. Technol.*, Oct. 2017, pp. 1–14.

[11] A. Yebi *et al.*, "Nonlinear model predictive control strategies for a parallel evaporator diesel engine waste heat recovery system," in *Proc. ASME Model. Control Automot. Syst.*, Oct. 2016, p. V002T19A003.

[12] J. Peralez, P. Tona, M. Nadri, P. Dufour, and A. Sciarretta, "Optimal control for an organic rankine cycle on board a diesel-electric railcar," *J. Process Control*, vol. 33, pp. 1–13, Sep. 2015. [Online]. Available: https://www.sciencedirect.com/science/article/pii/S0959152415000554

[13] O. C. Zienkiewicz, R. L. Taylor, O. C. Zienkiewicz, and R. L. Taylor, *The Finite Element Method*, vol. 3. London, U.K.: McGraw-Hill, 1977.

[14] C. W. Rowley, T. Colonius, and R. M. Murray, "Model reduction for compressible flows using POD and Galerkin projection," *Phys. D, Nonlinear Phenomena*, vol. 189, nos. 1–2, pp. 115–129, Feb. 2004.

[15] H.-X. Li and C. Qi, *Spatio-Temporal Modeling of Nonlinear Distributed Parameter Systems: A Time/Space Separation Based Approac*, vol. 50. New York, NY, USA: Springer, 2011.

[16] D. G. Zill, *Differential Equations With Boundary-Value Problems*. Appleton, WI, USA: Nelson Education, 2016.

[17] C. A. Fletcher, *Computational Galerkin Methods*. New York, NY, USA: Springer, 1984, pp. 72–85.

[18] T. Bui, "Explicit and implicit methods in solving differential equations," Univ. Connecticut, Mansfield, CT, USA, 2010.